CONF-961202--14

Presented at Fall Meeting of the Materials Research Society, Boston, MA, December 2–6, 1996 and published in *Proceedings*

Synthesis, Optical Properties, and Microstructure of Semiconductor Nanocrystals Formed by Ion Implantation

J. D. Budai, C. W. White, S. P. Withrow, R. A. Zuhr, and J. G. Zhu
Solid State Division, Oak Ridge National Laboratory
P.O. Box 2008, Oak Ridge, Tennessee 37831-6030

prepared by
SOLID STATE DIVISION
OAK RIDGE NATIONAL LABORATORY
Managed by
LOCKHEED MARTIN ENERGY RESEARCH CORP.
under
Contract No. DE-AC05-96OR22464
with the
U.S. DEPARTMENT OF ENERGY
Oak Ridge, Tennessee

December 1996

DISCLAIMER

SYNTHESIS, OPTICAL PROPERTIES, AND MICROSTRUCTURE OF SEMICONDUCTOR NANOCRYSTALS FORMED BY ION IMPLANTATION

J. D. BUDAI, C.W. WHITE, S.P. WITHROW, R.A. ZUHR, AND J. G. ZHU
Oak Ridge National Laboratory, Oak Ridge, TN 37831-6030

ABSTRACT

High-dose ion implantation, followed by annealing, has been shown to provide a versatile technique for creating semiconductor nanocrystals encapsulated in the surface region of a substrate material. We have successfully formed nanocrystalline precipitates from groups **IV** (Si, Ge, SiGe), **III-V** (GaAs, InAs, GaP, InP, GaN), and **II-VI** (CdS, CdSe, CdS_xSe_{1-x}, CdTe, ZnS, ZnSe) in fused silica, Al_2O_3 and Si substrates. Representative examples will be presented in order to illustrate the synthesis, microstructure, and optical properties of the nanostructured composite systems. The optical spectra reveal blue-shifts in good agreement with theoretical estimates of size-dependent quantum-confinement energies of electrons and holes. When formed in crystalline substrates, the nanocrystal lattice structure and orientation can be reproducibly controlled by adjusting the implantation conditions.

INTRODUCTION

Recent advances in controlling and characterizing semiconductor nanocrystals and quantum dots has generated considerable interest in exploring new synthesis techniques and applications [1, 2]. Existing applications include commercially available optical filters [3], while promising potential applications range from quantum dot lasers to high-speed nonlinear optical switches. Several successful approaches have been developed for producing nanostructured materials, including arrested precipitation in solvents, controlling surface clusters during film growth, and lithographic etching. In addition, several research groups have initiated investigations into the formation of semiconductor nanocrystals using ion implantation [4 - 8]. In this approach, a supersaturated solid solution is produced by implantation into the surface region of a host material and nanocrystals are formed by precipitation either during high-temperature implantation or during subsequent thermal annealing. The formation and growth of precipitates in such a supersaturated solid solution follows a two-stage kinetic process described theoretically by Lifshitz and Slyozov (LS) [9, 10]. After an initial diffusion-limited nucleation stage, particle coarsening occurs by Ostwald ripening, where the larger particles grow at the expense of the smaller ones.

Much of the initial interest in ion-implanted semiconductor precipitates was focused on studies of the strong visible photoluminescence (PL) arising when indirect bandgap Si (or Ge) precipitates are formed by implantation in SiO_2 [5 - 8, 11]. This system is structurally related to porous silicon formed by electrochemistry, and the optical properties are also quite similar. The ion-implantation technique has since been extended to include the formation of compound semiconductor nanocrystals in SiO_2, Al_2O_3, and Si matrices [12, 13]. Such systems provide great opportunities for tailoring the composite materials properties since both direct and indirect compounds with a wide range of band gap energies are available. Table I

displays the semiconductor nanocrystals which we have synthesized at ORNL by ion implantation into three technologically-important substrate materials.

Table 1. Semiconductor nanocrystals grown by ion implantation. Y indicates nanocrystals formed. N indicates nanocrystals not observed. No symbol indicates systems not yet investigated.

	SUBSTRATE		
Nanocrystal	SiO_2	Al_2O_3	Si
Si	Y	Y	-
Ge	Y	Y	
SiGe	Y	Y	
GaAs	Y	Y	Y
GaP	Y		Y
GaN	N	Y	N
InP	Y		Y
InAs	Y		Y
CdS	Y	Y	Y
CdSe	Y	Y	Y
$CdSe_{0.5}S_{0.5}$	Y		
CdTe			Y
$CdSe_{0.5}Te_{0.5}$			Y
ZnS	Y		
ZnSe	Y		

Ion implantation offers several advantages, as well as challenges, as a technique for synthesizing nanocrystals. First, ion implantation is versatile, since almost any ion can be implanted into any solid substrate with extreme chemical purity, including isotopic discrimination. In some cases, this versatility may in fact provide a unique route for incorporating precipitates in substrates with particular chemical sensitivity or extreme melting temperatures. Second, ions are embedded directly in the matrix by implantation and hence the crucial steps of nanocrystal encapsulation or passivation are typically integral parts of the synthesis. Third, implantation can be carried out through masks or with focused beams, and hence is capable of creating well-defined, high-resolution patterns of regions containing quantum dots. Fourth, the quenching of the kinetic energy for implanted ions is an intrinsically metastable process and hence presents opportunities for unique kinetic routes to nonequilibrium structures. Finally, since ion implantation represents an integral part of existing semiconductor fabrication technology, improvements in equipment capabilities will continue and it will be relatively straightforward to incorporate quantum dots created by ion implantation into electronic devices.

Considering the challenges, ion implantation often introduces structural damage into the substrate. As will be demonstrated in this paper, the ion damage

itself sometimes provides useful changes in the host material. However in many cases, it must be controlled by high-temperature implantations or subsequent thermal annealing. In addition, since the implantation approach for creating nanocrystals relies on nucleation and Ostwald ripening of precipitates, the particles possess a range of sizes. Thus, applications requiring greater monodispersity will involve more complex thermal processing steps or advanced techniques such as writing individual quantum dots with finely focused ion beams [14].

EXPERIMENTAL

Semiconductor nanocrystals were formed by implantation of the constituent ions into several different host materials, including fused silica (Corning 7940 glass), silica grown by thermal oxidation on silicon wafers (SiO_2/Si), α-Al_2O_3(0001), and Si(001) wafers. Doses ranged up to ~$10^{17}/cm^2$ for each species, and the ion energies were chosen such that the ion concentration profiles were superimposed after implantation. As expected, the size of the nanocrystals increased when the substrate temperature was increased, either during implantation or during subsequent annealing in flowing Ar + 4% H_2. The implanted samples were characterized by Rutherford backscattering (2.3 MeV He ions), four-circle x-ray diffraction (Cu$K\alpha_1$), transmission electron microscopy (TEM), optical absorption, photoluminescence (PL), and Raman spectroscopy.

RESULTS AND DISCUSSION

I. OPTICAL PROPERTIES OF II-VI NANOCRYSTALS IN SiO_2

Silica glasses obviously represent an important class of optical materials and extensive efforts have been made throughout history to modify their properties through the addition of various forms of impurities or inclusions. We have succeeded in creating a wide range of elemental and compound semiconductor nanocrystals embedded in fused silica by implantation and thermal annealing. In general, precipitation in a glassy matrix results in the formation of spherical, randomly oriented, nanocrystals. Here, we present representative results for CdS, a direct bandgap II-VI compound formed in SiO_2. Semiconductor nanocrystals were formed by ion implantation of the constituent group II and group VI ions into bulk fused silica, or into a thermally oxidized silica layer grown on a silicon wafer.

Figure 1 shows x-ray diffraction θ-2θ scans obtained from samples implanted at room temperature with $1 \times 10^{17}/cm^2$ at a single energy for each of the group II and group VI ions, and subsequently annealed at 1000°C for one hour in an Ar/ 4% H_2 atmosphere. The measurements show that randomly oriented, CdSe and CdS precipitates are formed predominantly in the hexagonal wurtzite structure. The positions of the diffraction peaks for the Cd+0.5Se+0.5S sample lie intermediate between the pure compounds, indicating that the mixed compound $CdSe_{0.5}S_{0.5}$ has been formed. This conclusion is further supported by Raman spectra.

The optical properties of the CdS sample described above is shown in Figure 2, with the absorption and PL spectra shown on the left and right sides respectively. After annealing at 1000°C, the absorption spectra develops steep band-edge structure near the bulk value of the CdS bandgap (2.43 eV = 510 nm at room

temperature). We attribute the higher energy peak in the PL spectra to bound excitonic recombination within the CdS nanocrystals and the broad, lower energy peak ($\lambda > 650$ nm) to surface-related interface states. Similar absorption features have been observed in doped bulk-glasses containing CdS nanoparticles formed during heat treatments [15], as well as in commercially available Cd(S,Se) glass filters [3, 16]. In addition, we have observed similar results for CdSe, ZnS, and ZnSe nanocrystals formed in SiO_2 by ion implantation. The broad, lower energy PL peak has been observed to strengthen significantly with temperatures above 45K in CdSeS samples [16], consistent with the relatively intense peak found in our room-temperature measurements. We note however, that unlike our observations, some previous studies of CdS nanoparticles in filter glasses failed to detect measurable PL near the direct bandgap energy [3]. This difference may be due to the high Cd and S concentrations and high-temperature heat treatments used in our work.

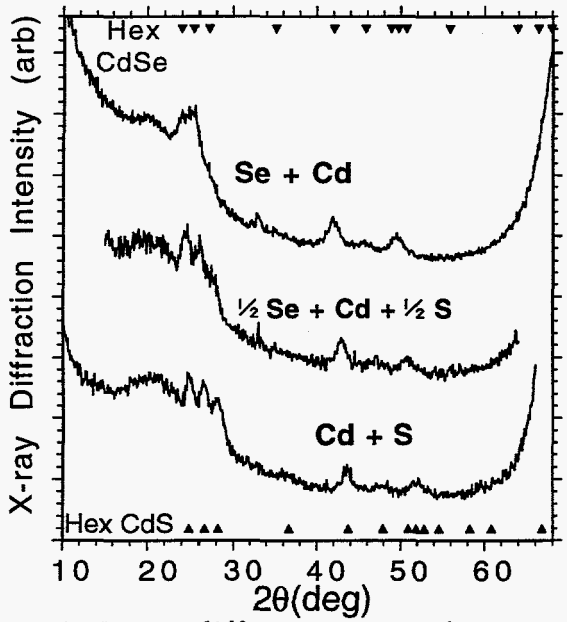

Fig. 1. X-ray diffraction scans from II-VI nanocrystals in a SiO_2 layer on Si. The implantation energies used were Cd(450 keV); Se(330 keV); S(164 keV).

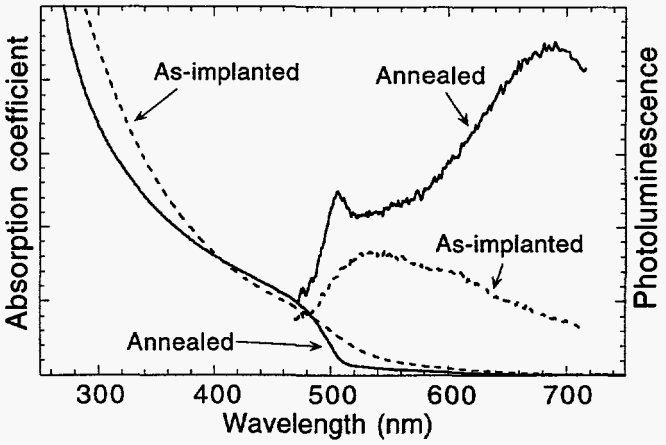

Fig. 2. Optical absorption (left side) and photoluminescence (right side) from a CdS in SiO_2 sample before and after annealing at 1000°C.

The results presented in Fig. 1 and Fig. 2 were obtained from samples synthesized using a single energy for each ion species, resulting an approximately Gaussian concentration depth profile for the implanted ions. After annealing, TEM images show relatively broad distributions of particle sizes, with the largest precipitates located near the peak position of the concentration profile, and the smallest in the tails. Thus, the optical results represent a convolution of spectra from particles with a wide range of sizes. In order to obtain more constant concentration profiles and hence more uniform particle-size distributions, samples were synthesized by implanting ions at three different energies (Cd ions at 35, 120, and 320 keV; S ions at 35, 60, and 110 keV). These energies yielded a relatively uniform concentration of ions in a ~1500Å surface layer. After high-temperature annealing, the late-stage particle-size distributions in these 'flat-profile' samples is

controlled by Ostwald ripening [9, 10], where the average particle volume is proportional to the excess concentration.

Figure 3 shows the optical absorption coefficient, α, measured after annealing at 1000°C for one hour from four 'flat-profile' samples with different excess concentrations ranging from $4 \times 10^{20}/cm^3$ (~0.5 at %) to $6.3 \times 10^{21}/cm^3$ (~8 at %) for each of the implanted Cd and S ion species. As the concentration is decreased, the absorption threshold shifts towards shorter wavelength, as expected from quantum-size effects due to confinement of an electron and hole in nanocrystals smaller than the exciton Bohr diameter (~50Å for CdS). Our absorption spectra do not exhibit a distinct exciton peak as is often observed for semiconductor nanocrystal systems. This feature will be broadened by our relatively large size-distribution as well as the measurement temperature (RT), and our observations are consistent with previous findings [17] for S-rich Cd(Se,S) nanocrystals in doped SiO_2.

Since CdS is a direct band gap material, we can extract an experimental estimate of the gap, Eg, from the intercept value of a plot of $(\alpha E)^2$ vs. E, where E is the photon energy [18]. Applying this procedure to the data in Fig. 3 yields blue shifts, $\Delta Eg = Eg - Eg(bulk)$, of up to ~0.3 eV compared with the bulk CdS band gap of ~2.43 eV. A theoretical estimate of the confinement energy, ΔEg, as a function of a spherical particle diameter, d, using the effective-mass approximation has been given by Brus [19]:

$$\Delta Eg(d) = (2\hbar^2\pi^2/\mu d^2) - (3.6e^2/\varepsilon d) \qquad (1)$$

where $\hbar$ is Planck's constant, μ is the exciton reduced mass ($\sim 0.154 m_o$), e is the electron charge, and ε is the dielectric constant (~8.9). Inverting this theoretical expression, we have obtained predicted particle sizes for each of the four experimentally determined values of ΔEg. A tight-binding approximation calculation of $\Delta Eg(d)$ for CdS has been used to generate a curve similar in functional shape to equation (1), but quantitatively shifted [20].

Considering the expected dependence of the particle size on implantation dose, the Ostwald ripening process described by LS theory predicts an average particle volume, $(\pi d^3/6)$, which increases proportionately with the excess concentration, c_o. Thus $d \sim c_o^{1/3}$, and Fig. 4 shows the approximate particle diameters obtained from equation (1) plotted as a function of $(concentration)^{1/3}$ for the four CdS samples. An approximately linear relation is observed, in spite of the fact that the LS treatment is strictly valid only in the limit of dilute concentrations where there are no interparticle diffusion interactions.

Note that the particle diameters displayed in Fig. 4 were estimated indirectly from the measured shifts of the absorption spectra. Direct TEM and x-ray diffraction measurements of the particle sizes for comparison are not yet available for these particular 'flat profile' CdS samples. However, we have measured the particle size distribution from the central region of a single energy CdS in SiO_2/Si sample, in which the peak concentration was calculated to be $\sim 8 \times 10^{21}/cm^3$. As discussed above, the highest concentration region for this sample possesses the largest nanocrystals and the particle size distribution in this region should be similar to that for the more uniform 'flat profile' sample with a similar excess concentration. The FWHM range of particle diameters for the central region of this sample is indicated

on Fig. 4 with the midpoint marked by the open circle. This observation is in excellent qualitative agreement with the diameters extracted from the energy shifts, especially when one considers that the experimental optical properties are generally volume-weighted, and will be dominated by the largest nanocrystals. When the TEM distribution is weighted by the particle volumes, the midpoint is shifted to ~100Å, as indicated by an × in Fig. 4.

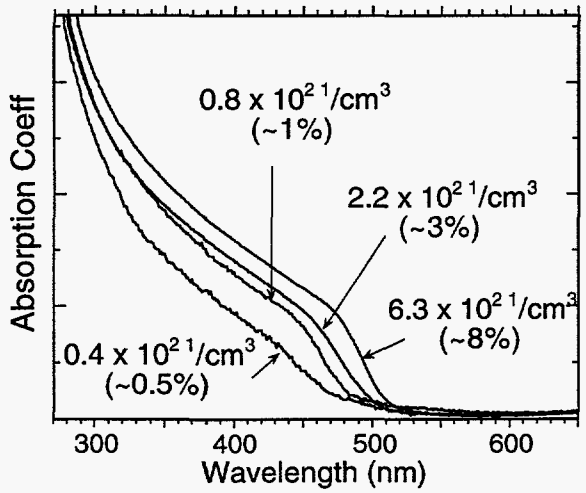

Fig. 3 Optical absorption for four samples implanted with Cd and S ions at multiple energies to produce uniform concentration profiles. The samples were all annealed at 1000°C for one hour.

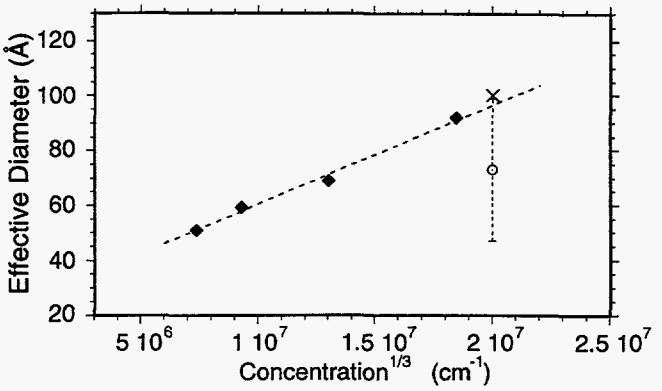

Fig. 4 The estimated CdS particle diameters calculated from equation (1) for different doses are marked by ◆. The open circle indicates the midpoint of a TEM measurement from a similar sample. The × indicates the TEM volume-weighted midpoint.

II. CONTROLLING NANOCRYSTALS IN Al_2O_3 USING ION DAMAGE

In contrast to the previous section, precipitation within a crystalline matrix generally results in the formation of crystallographically oriented precipitates, often with faceted shapes. We have previously reported the synthesis and preliminary optical properties of both elemental and compound semiconductor nanocrystals in α-Al_2O_3 [4, 12]. Here, we describe microstructural changes in semiconductor nanocrystals formed in Al_2O_3 associated with the accumulation of lattice damage in the substrate.

Figure 5 shows θ-2θ x-ray scans along the α-$Al_2O_3(000\ell)$ axis for six different combinations of ion species, after single-energy ion implantation and subsequent annealing, with a representative range of doses, substrate implantation-temperatures, and post-implant annealing temperatures: **Si**(400 keV, $6 \times 10^{17}/cm^2$, 650°C), anneal 1100°C; **Ge**(500 keV, $1.5 \times 10^{17}/cm^2$, RT), anneal 900°C; **Ge**(500 keV, $6 \times 10^{16}/cm^2$, 550°C) + **Si**(215 keV, $6 \times 10^{16}/cm^2$, 550°C), anneal 900°C; **As**(500 keV, $1 \times 10^{17}/cm^2$, LN_2) + **Ga**(470 keV, $1 \times 10^{17}/cm^2$, LN_2), anneal 1100°C; **Se**(330 keV, $4.3 \times 10^{16}/cm^2$, 600°C) + **Cd**(450 keV, $4.3 \times 10^{17}/cm^2$, 600°C), anneal 1000°C; and **Cd**(450 keV, $4.3 \times 10^{16}/cm^2$, 600°C) + **S**(215 keV, $4.3 \times 10^{16}/cm^2$, 600°C), anneal 1000°C.

These x-ray scans reveal that, in general, only a few diffraction peaks appear in addition to the intense substrate α-$Al_2O_3(0006)$ peak. The peak which appears in

all scans in the range $2\theta \sim 25°\text{-}30°$ is due to the precipitation of oriented semiconductor nanocrystals in the usual diamond cubic, hexagonal wurtzite, or cubic zincblende structures. These phases are structurally related, with an ABABAB plane-stacking sequence corresponding to the hexagonal $(0001)\perp$ structure and an ABCABC stacking sequence corresponding to the cubic $(111)\perp$ structures. The observed alignment of the hexagonal (0001) planes or the cubic (111) planes of the nanocrystals with the pseudo-hexagonal substrate (0001) planes is predicted from simple symmetry considerations. The intensity and width of this peak for particular implanted species depends on the number and size of the precipitates, and as expected, larger particles are produced by higher ion doses or higher temperatures (enhanced ripening).

In addition to the nanocrystal peaks, a series of diffraction peaks corresponding to an aligned γ-phase of Al_2O_3 is often observed. These peaks are labeled γ in Fig. 5 in the Ge and the Ga+As implanted samples. However, the presence or absence of the γ-phase x-ray peaks does not depend on the particular implanted ion species. Instead, the γ-phase is observed with any of the ion species whenever the substrate temperature during implantation is relatively low (typically room temperature or below) and the dose is sufficiently high. In such cases, the accumulated lattice-displacement damage due to the implanted ions is sufficient to amorphize the surface layer of the α-Al_2O_3 substrate. Subsequent thermal annealing is known to consist of a two-step recrystallization process [21-24]. An amorphous Al_2O_3 layer on sapphire recrystallizes during annealing first as an epitaxial, metastable γ-phase layer, and then transforms back to the original α-phase at a still higher temperature via layer-by-layer growth modes. The intermediate γ-phase consists of a cubic stacking sequence (ABCABC) variant of Al_2O_3 which has been hypothesized to be stabilized by the greater potential for defect accommodation in the γ-phase. The recrystallization into γ-Al_2O_3 occurs epitaxially with an orientation relation given by $\gamma(111)[1\bar{1}0] \parallel \alpha(0001)[10\bar{1}0]$ or the associated 60° rotated domains. Experimentally, we find that the amorphization dose and the regrowth kinetics depend strongly on the particular implanted impurities, but that the general microstructural evolution is the same for all implanted semiconductor species illustrated here.

The presence of intermediate γ-phase recrystallization in Al_2O_3 substrates leads to several interesting microstructural changes in the precipitated semiconductor nanocrystals, including changes in the orientation. Figures 6(a) and 6(b) show x-ray diffraction θ–2θ-scans taken from two α-Al_2O_3 samples implanted with the same energies and doses of Ge(500 keV, $6 \times 10^{16}/cm^2$) and Si(220 keV, $6 \times 10^{16}/cm^2$) and subsequently annealed for one hour at 1100°C. The only difference in the synthesis of these two samples was in the substrate temperature during implantation; for Fig 6(a) the substrate was held at an elevated temperature of 550°C, while for Fig. 6(b) the substrate was at room temperature (RT). The positions of the nanocrystal (111) peaks show that alloy SiGe nanocrystals (as opposed to separate Si or Ge nanocrystals) are formed in both samples with their diamond cubic (111) planes parallel to the substrate (0001) planes. In Fig. 6(a), although some lattice damage may be present, the elevated temperature of 550°C provides sufficient dynamic annealing that the substrate remains α-phase. Only the α-Al_2O_3(0006) and the SiGe(111) alloy peaks are observed. In contrast, the lattice

damage in the RT-implanted sample accumulated to the point that the surface layer of the substrate was amorphized, as verified by Rutherford backscattering. Subsequent annealing produced γ-phase regrowth as shown in Fig 6(b).

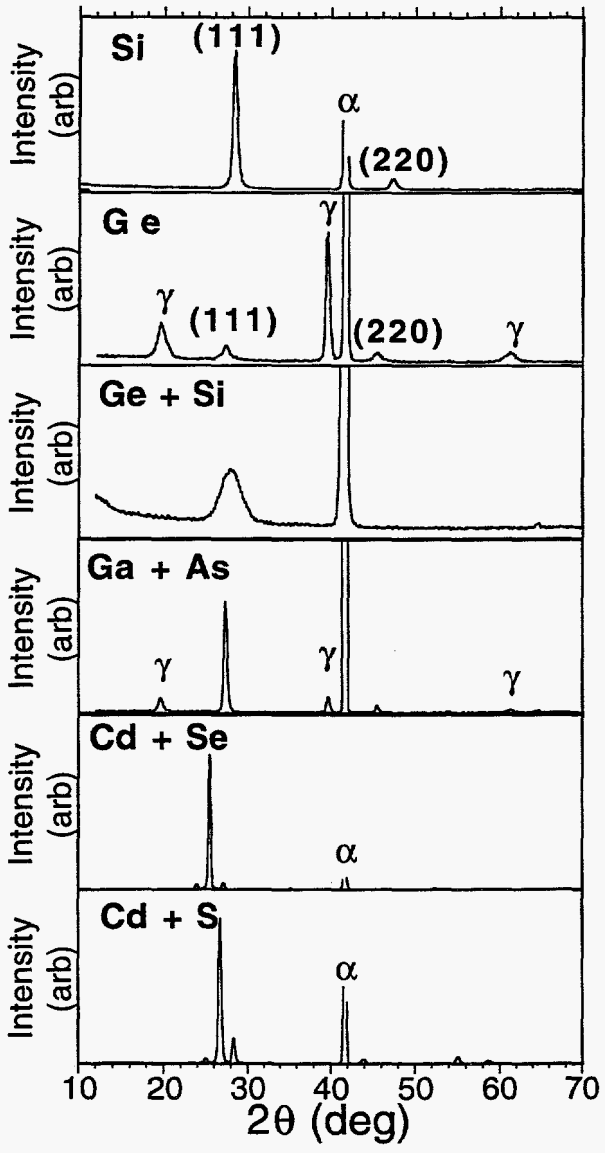

Figure 5 θ-2θ x-ray scans for α-Al_2O_3(0001) implanted with six different combinations of ions. Implant temperatures, energies and doses, and annealing conditions are given in the text.

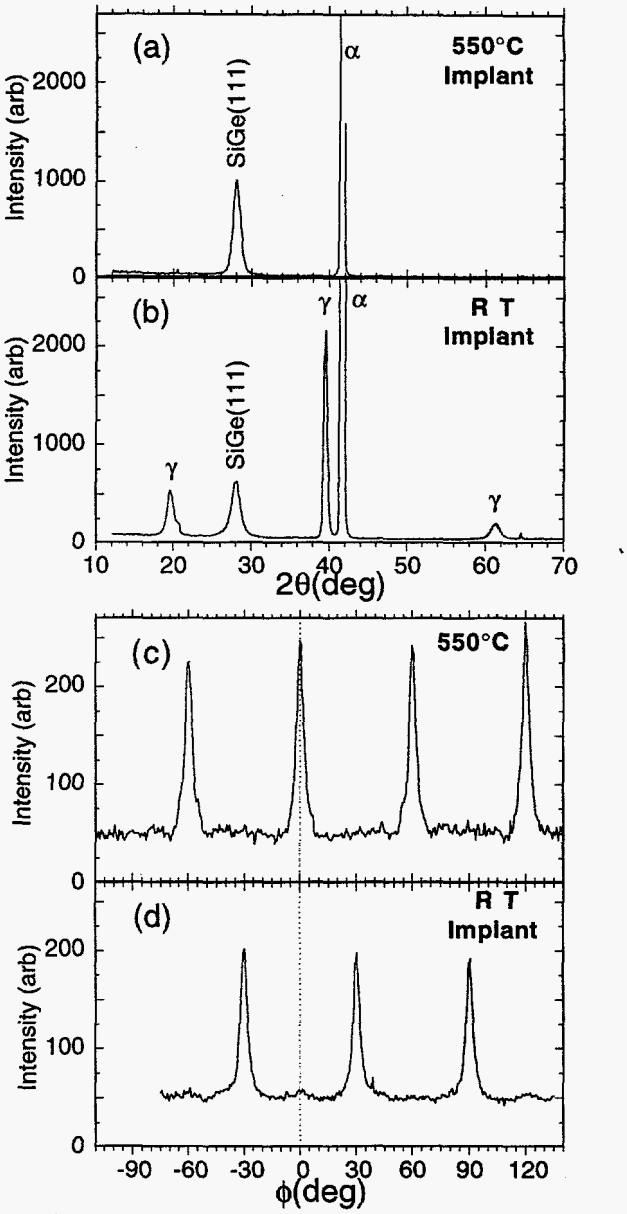

Figure 6 (a,b) X-ray θ-2θ scans for α-Al_2O_3 implanted with Ge + Si with substrate temperatures of (a) 550°C and (b) Room Temp during implantation. (c,d) X-ray φ scans showing nanocrystal orientation for the same samples: (c) 550°C and (d) Room Temp

The large microstructural difference in Al_2O_3 substrates implanted at different temperatures has a direct effect on the semiconductor nanocrystal orientation as illustrated in Figures 6(c) and 6(d). These figures show x-ray φ-scans

using the SiGe{220} reflections, and indicate the in-plane nanocrystal orientations for the same samples used in Figures 6(a) and 6(b). For the sample implanted at 550°C, the in-plane orientation is described by SiGe[$1\bar{1}0$] ‖ α-Al_2O_3[$11\bar{2}0$] (and 60° rotated domains), whereas for the sample implanted at RT, the nanocrystals are rotated by ±30° away from this orientation. The orientations are distinct for these two samples because the SiGe nanocrystals were nucleated and grew while embedded in an α-Al_2O_3 matrix in one case, and were nucleated within a γ-Al_2O_3 matrix in the other. Although illustrated here with SiGe, this orientational dependence on substrate microstructure is a general phenomena and is observed for the other semiconductor nanocrystals. If samples containing γ-oriented nanocrystals (such as used in Fig 6(b) and 6(d)) are subsequently annealed at higher temperatures or longer times such that the γ-Al_2O_3 layer is transformed back to α-Al_2O_3 without melting the nanocrystals, then the nanocrystals remain and coarsen in the γ-orientation in which they were originally formed. Thus, it is possible to reproducibly create nanocrystals oriented in either of the two directions within an α-Al_2O_3 substrate.

CONCLUSIONS

We have synthesized a wide range of semiconductor nanocrystals encapsulated in SiO_2, α-Al_2O_3 and Si substrates using ion implantation and thermal annealing. The particle-size distribution is changed by controlling the processing conditions such as the ion dose and the annealing temperature. Nanocrystals are typically spherical in shape and randomly oriented when precipitated within an amorphous matrix such as SiO_2, and are faceted and oriented in crystalline hosts such as Al_2O_3 and Si. Strong visible photoluminescence has been observed from some systems, and the absorption spectra show quantum-confinement blue-shifts in good agreement with size-dependent theoretical estimates. Interesting microstructural effects related to substrate ion damage have been observed for nanocrystals formed in α-Al_2O_3. Damage accumulation in low-temperature implants produces an amorphous Al_2O_3 surface layer, which recrystallizes during subsequent thermal annealing as an epitaxial, metastable γ-phase Al_2O_3 layer. Nanocrystals which nucleate within γ-Al_2O_3 are found to be microstructurally distinct from those nucleated within α-Al_2O_3.

ACKNOWLEDGMENT

This research sponsored by the Division of Materials Sciences, U.S. Department of Energy under Contract No. DE-AC05-96OR22464 with Lockheed Martin Energy Research Corp.

REFERENCES

1. A.P. Alivisatos, Science **271**, 933 (1996).

2. Special issue: Chemistry of Materials, vol. 8, no. 8 (1996).

3. N.F. Borrelli, D.W. Hall, H.J. Holland, and D.W. Smith, J. Appl. Phys. **61**, 5399 (1987).

4. C.W. White, J.D. Budai, S.P. Withrow, S.J. Pennycook, D.M. Hembree, D.S. Zhou, T. Vo-Dinh, and R.H. Magruder, *Mat. Res. Soc. Symp. Proc.* **316**, 487 (1994).

5. H.A. Atwater, K.V. Shcheglov, S.S. Wong, K.J. Vahala, R.C. Flagan, M.L. Brongersma, and A. Polman, *Mat. Res. Soc. Symp. Proc.* **316**, 409 (1994).

6. T. Shimizu-Iwayama, K. Fujita, S. Nakao, K. Saitoh, T. Fujita, and N. Itoh, J. Appl. Phys. **75**, 7779 (1994).

7. T. Komoda, J.P. Kelly, A. Nejim, K.P. Homewood, P.L.F. Hemment, and B.J. Sealy, *Mat. Res. Soc. Symp. Proc.* **358**, 163 (1995).

8. P. Mutti, G. Ghislotti, S. Bertoni, L. Bonoldi, G. Cerofolini, L. Meda, E. Grilli, and M. Guzzi, Appl. Phys. Lett. **66**, 851 (1995).

9. I.M. Lifshitz and V.V. Slyozov, J. Phys. Chem. Solids **19**, 35 (1961).

10. P.W. Voorhees, *Annu. Rev. Mater. Sci.* **22**, 197 (1992).

11. J.G. Zhu, C.W. White, J.D. Budai, S.P. Withrow, and Y. Chen, *Mat. Res. Soc. Symp. Proc.* **358**, 175 (1995).

12. C.W. White, J.D. Budai, J.G. Zhu, S.P. Withrow, R.A. Zuhr, D.M. Hembree, D.O. Henderson, A. Ueda, Y.S. Tung, R. Mu, and R.H. Magruder, J. Appl. Phys. **79**, 1876 (1996).

13. C.W. White, J.D. Budai, J.G. Zhu, S.P. Withrow, and M.J. Aziz, Appl. Phys. Lett. **68**, 2389 (1996).

14. L. Feldman, private communication.

15. V. Sukumar and R.H. Doremus, phys. stat. sol. (b) **179**, 307 (1993).

16. J. Warnock and D.D. Awschalom, Phys. Rev. B **32**, 5529 (1985).

17. Y. Fuyu and J. M. Parker, Materials Letters **6**, 233 (1988).

18. J.I. Pankove, Optical Processes in Semiconductors, Dover Publications, New York, 1971.

19. L. E. Brus, J. Chem. Phys. **80**, 4403 (1984).

20. P.E. Lippens and M. Lannoo, Phys. Rev. B **39**, 10935 (1989).

21. C.W. White, C.J. McHargue, P.S. Sklad, L.A. Boatner, and G.C. Farlow, Materials Science Reports **4**, 41 (1989).

22. C.W. White, L.A. Boatner, P.S. Sklad, C.J. McHargue, J. Rankin, G.C. Farlow, and M.J. Aziz, Nucl. Instr. Methods B **32**, 11 (1988).

23. N. Yu, P.C. McIntyre, M. Nastasi, and K.E. Sickafus, Phys. Rev. B **52**, 17518 (1995).

24 S. Cao, A.J. Pedraza, D.H. Lowndes, and L.F. Allard, Appl. Phys. Lett. **65**, 2940 (1994).